Applied Surface Science 512 (2020) 145649

Contents lists available at ScienceDirect

Applied Surface Science

journal homepage: www.elsevier.com/locate/apsusc

Full Length Article

Epitaxial vanadium nanolayers to suppress interfacial reactions during deposition of titanium-bearing Heusler alloys on MgO(0 0 1)

R.W.H. Webster[a,*], M.T. Scott[a], S.R. Popuri[b], J.W.G. Bos[b], D.A. MacLaren[a,*]

[a] SUPA, School of Physics and Astronomy, University of Glasgow, Glasgow G12 8QQ, United Kingdom
[b] Institute of Chemical Sciences and Centre for Advanced Energy Storage and Recovery, School of Engineering and Physical Sciences, Heriot-Watt University, Edinburgh EH14 4AS, United Kingdom

ARTICLE INFO

Keywords:
Half-Heuslers
Thermoelectric
Contact layer
TEM
Thin-fim
Epitaxy

ABSTRACT

Epitaxial growth of the half-Heusler alloy TiNiSn onto (1 0 0)-oriented MgO is compromised by interfacial reactions driven by the oxidising potential of titanium. Here, we demonstrate that a few epitaxial monolayers of elemental vanadium are sufficient to act as an impermeable buffer that maintains epitaxy and stoichiometric thin film growth but suppresses interfacial oxidation of the alloy. Electron diffraction and microscopy are used to characterise the thin film morphologies and thereby determine the optimum deposition conditions. Electron energy loss spectroscopy is used to demonstrate the chemical nature of the resulting thin film interfaces and confirms that TiNiSn film quality is improved.

1. Introduction

In the effort to produce commercially-viable thermoelectric generators that don't rely on scarce elements, Heusler alloys have attracted much interest owing to their versatility and capacity for tunability. For the half-Heusler (hH) TiNiSn, which is a candidate n-type thermoelectric, its rich compositional phase-space has been exploited to improve thermoelectric properties [1–5] and there is considerable scope for tuning the performance through doping [6–8]. However, the integrity of the alloy can be compromised by the presence of even trace amounts of oxygen [9], due to the gettering properties of elements like titanium, vanadium, zirconium and hafnium, all of which have been explored as dopants in TiNiSn and are common elemental components of other Heusler alloys [10]. Recently, we reported on the pulsed laser deposition of TiNiSn upon single-crystalline MgO to produce near-stoichiometric, mono-crystalline, epitaxial films [11]. However, we also observed a deleterious reaction that maintained epitaxy but drew Ti out of the alloy. The subsequent formation of a thin TiO interfacial layer limited the availability of Ti for the intended film and introduced a compositional perturbation that took upwards of 10 nm of further deposition to recover. In addition, some Ti was observed to diffuse several nanometres into the substrate, consistent with facile diffusion by cation substitution mechanisms reported elsewhere [12].

Here, we explore the use of a non-oxide buffer layer to prohibit the interfacial reaction and diffusion found previously and thereby lead to better maintenance of the hH stoichiometry upon deposition. We examine the use of elemental vanadium which, with a lattice constant of 3.024 Å for the (0 0 1) direction of its bcc unit cell [13], has a near-coincident lattice match with both MgO and TiNiSn through a 45° rotation of the unit cell about the (0 0 1) axis of the MgO, as established previously in studies of magnetic tunnel junctions [14] and, more pertinently, for the use of contact electrodes with half-Heuslers [15]. Fig. 1 illustrates the nature of this potential epitaxial relationship, based on a lattice mismatch of + 1.5% between V and MgO and of −1.9% between V and TiNiSn (deriving from bulk lattice constants of 4.212 Å [16] and 5.935 Å [17], respectively, for MgO and TiNiSn). Rather than the thick electrodes studied previously [15], here we consider a thin buffer layer that is only a few nanometres thick and grown by dc magnetron sputter deposition. Since the formation of buried epitaxial oxides is effectively invisible to diffractive techniques, we focus on a chemical analysis of the interfacial region using a cross-sectional sample. We employ electron energy loss spectroscopy (EELS) in scanning transmission electron microscopy (STEM) to provide chemical discrimination on the sub-nanometre scale. Our studies confirm the good crystallographic quality of the hH film, which has a structure which appears consistent with the $F\bar{4}3m$ space group [18], and demonstrate that diffusion of titanium and oxygen across the film-substrate interface is suppressed by just a few nanometres of epitaxial vanadium: an outcome of relevance to the deposition of other Heusler and titanium-bearing alloys on MgO substrates. We also note that the V does not form additional alloy phases with the TiNiSn in the

* Corresponding authors.
E-mail addresses: rwebster@physics.org (R.W.H. Webster), dmaclaren@physics.org (D.A. MacLaren).

https://doi.org/10.1016/j.apsusc.2020.145649
Received 17 October 2019; Received in revised form 10 January 2020; Accepted 3 February 2020
Available online 04 February 2020
0169-4332/ © 2020 The Authors. Published by Elsevier B.V. This is an open access article under the CC BY license (http://creativecommons.org/licenses/by/4.0/).

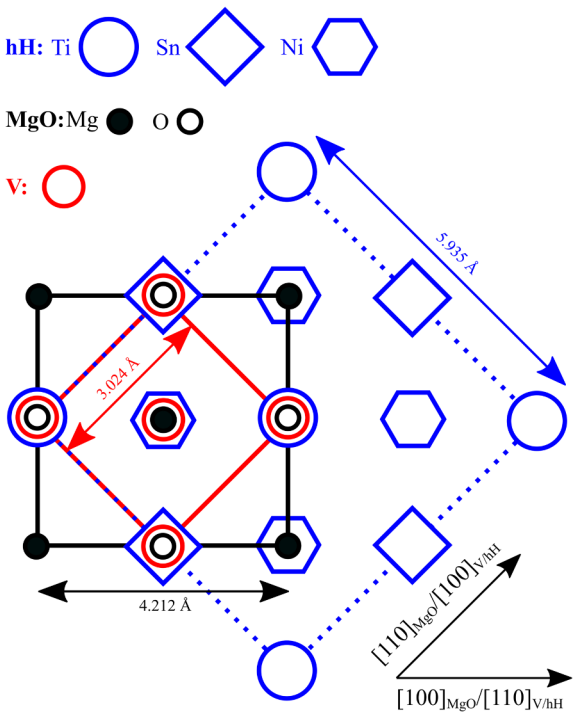

Fig. 1. Schematic illustrating the nature of epitaxial relationship between the unit cells of MgO, V and TiNiSn. The boundary of each unit cell is outlined and the lattice constants of each material labelled.

temperature range explored here, which suggests that it may have practical significance as a barrier layer when TiNiSn alloys are used in thermoelectric modules, both to minimise atmospheric oxidation and to prevent reactions with electrode materials.

2. Materials and methods

Thin films of TiNiSn were deposited via Pulsed Laser Deposition (PLD) in a Neocera Pioneer vacuum system using a KrF excimer laser (248 nm, 20 ns pulse duration, typically 200 mJ/pulse at 20 Hz). Deposition was monitored by reflection high energy electron diffraction (RHEED) and carried out with a substrate temperature of 670 K at the base pressure of the vacuum chamber, typically 10^{-8} Torr, in line with our own recent studies optimising the growth of TiNiSn thin films on single crystal MgO [11]. The target material for laser ablation was a sintered, Ni-rich TiNiSn disc with an approximate composition of 1:1.1:1 and prepared by solid state reactions [4].

Vanadium (99.9 + %, Pi-Kem Ltd, UK) was deposited *in situ* in the PLD chamber by dc-magnetron sputtering using an argon background with a partial pressure of 2.5 – 25 mTorr and substrate temperatures ranging from 298 to 823 K. The vanadium target was sputtered prior to deposition to remove any oxide scale which may have formed on the target surface. MgO(0 0 1) single-crystal substrates (Pi-Kem Ltd, UK) with a typical peak-to-peak roughness of 4 Å (as measured by atomic force microscopy, AFM – see below) were annealed *in situ* under ultra-high vacuum conditions at 970 K for at least 1 h prior to any deposition to remove carbonaceous contaminants that may have adsorbed on the surface [19], though at the expense of introducing a small amount of surface rumpling [20]. AFM was performed on a Bruker Dimension instrument in tapping mode and the relative surface roughness was assessed with a crude RMS value, calculated using a $(5\ \mu m)^2$ scan with 512 pixel resolution after removal of a background polynomial.

Cross-sections of thin film samples for transmission electron microscopy (TEM) studies were prepared using a ThermoFischer Helios Dualbeam plasma focused ion beam (PFIB) instrument using routine procedures [21]. A probe-corrected JEOL ARM200cF instrument with a cold field emission source operated at 200 kV was used for acquiring TEM and STEM data. Spatially resolved chemical maps were obtained by EELS using a Gatan 965 Quantum ER post-column spectrometer to acquire STEM Dual-EELS spectrum images [22,23]. Quantification of elemental concentrations was carried out by a method of absolute quantification that employs experimentally obtained reference spectra from each element as components for a multiple-linear least-squares (MLLS) fit, as described elsewhere [24–26]. This method was used due to the proximity of the characteristic EELS edges that were of interest – Ti L (457 eV), Sn M (485 eV), V L (513 eV) & O K (532 eV) – which compromised standard quantification routines involving the subtraction of a pre-edge background. This effect was compounded by difficulties in using the Hartree-Slater scattering cross-sections, whose uncertainty may be as large as 20% for the quantification of M edges [27]. Geometric phase analysis of lattice-resolved images was performed using the Strain + + software package [28] to calculate differential phase maps using methods described by Hytch *et al* [29]. The same methods were also used to process the phase information present in STEM-moiré images [30].

3. Results and discussion

Although the sputter deposition rate inevitably reduces with gas pressure, we found that the highest Ar sputtering pressure used, 25 mTorr, produced the smoothest V films on MgO, independent of substrate temperature. For example, a 10 nm-thick film deposited at 298 K and a rate of order 0.05 nm s^{-1} had an average RMS surface roughness of 1.9 Å, which was a threefold improvement when compared to films prepared at 10 mTorr. Although little variation in the V film roughness was expected with temperature [13], AFM measurements of films grown between 298 K and 823 K indicated 623 K to produce the smoothest films and still gave rise to sharp RHEED features consistent with epitaxial growth (see below). In order to avoid potential roughening [31] or other phase transitions [13] that could arise when heating the deposited film, deposition temperatures initially considered were at, or above, the substrate temperature of 723 K intended for deposition of TiNiSn. However, we found that the sharp RHEED patterns observed at lower temperatures disappeared for vanadium grown above 673 K, so a lower deposition temperature was necessary. This is consistent with previous molecular beam epitaxy (MBE) work that demonstrated high quality epitaxial growth between 473 K and 673 K [13,32] but amorphous films at higher temperatures [13].

For pulsed laser deposition of the TiNiSn thin film atop the vanadium, the substrate temperature was increased to 723 K, to be consistent with our previous study [11]. There was no obvious degradation in V film crystallinity during heating, similar to earlier work [14] and we conclude that there is a difference between films grown at 723 K and those deposited at lower temperatures and annealed to 723 K: this may relate to disorder in the first few monolayers deposited at elevated temperatures, so that epitaxy is never established. PLD was then carried out in a 'burst' mode, whereby a quantity of pulses equivalent to one TiNiSn unit-cell of layer-thickness is delivered with a pulse frequency of 18 Hz, followed by a short 'annealing' phase of 10–20 s before the next burst begins. To deposit a film of approximately 20–25 nm thickness, 40 repetitions of this cycle were used. This thickness was sufficient to assess the growth mode and interface chemistry but thinner than that required for thermoelectric devices. Our previous work showed growth of TiNiSn directly onto MgO to initiate through the growth of flat islands that coalesce with thickness, as the film relaxes to its bulk lattice spacing [11]. We find that deposition onto the V buffer follows a similar mechanism, suggesting that the 3d growth mode is, indeed, driven more by strain effects than by surface diffusion kinetics, which would be expected to be different for deposition onto V rather than MgO. The RHEED patterns in Fig. 2 summarise the data collected during deposition. The pattern in Fig. 2(a) was recorded from the MgO substrate, and the vertical streaks observed are typical for a smooth surface with the

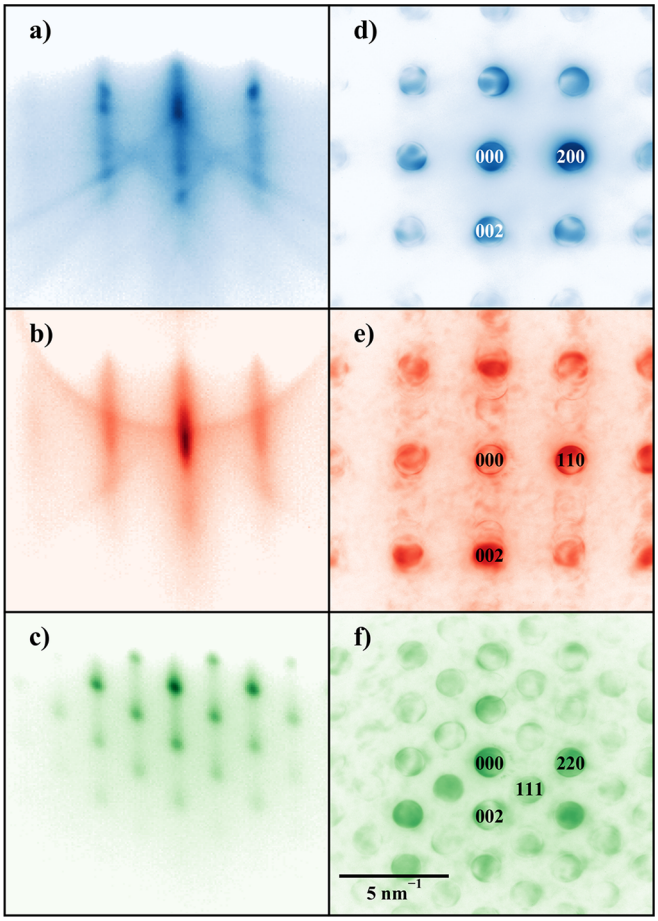

Fig. 2. RHEED patterns for (a) MgO, (b) vanadium and (c) TiNiSn surfaces collected during deposition of TiNiSn/V/MgO. (d-f) Cross-sectional TEM CBED patterns collected from the same layers after deposition, with the same scalebar. Miller indices for some reflections are indicated in (d-f), indexed with respect to the unit cells for MgO, V and hH structures, respectively.

main feature being atomic-scale terraces, which is consistent with the RMS roughness of 1.1 Å measured by AFM. The pattern in Fig. 2(b), collected from a 5 nm-thick vanadium film grown at 623 K, is similar to that seen for MgO, indicating the formation of a film with strong epitaxial quality and minimal surface roughening relative to the MgO surface; AFM shows the RMS roughness increases marginally to 1.6 Å. The pattern collected after deposition of ~ 25 nm of TiNiSn, shown in Fig. 2(c), differs in the appearance of discrete diffraction spots with a doubled periodicity, similar to the patterns collected in our previous TiNiSn/MgO deposition study and consistent with epitaxial growth of TiNiSn with lattice alignment as sketched in Fig. 1. The square symmetry is consistent with that of the $F\bar{4}3m$ unit cell; but we note that the limitations of dynamical diffraction makes the technique insensitive to a degree of exchange between sites in the hH lattice. The spotty rather than streaky pattern derives from transmission diffraction through a rough, 3-dimensional surface. The AFM-measured RMS roughness for this layer increases dramatically to 22.6 Å, consistent with a propensity for island growth in the initial stages of deposition; the islands are visualised directly by TEM below. Note that for the hH film, the RMS roughness becomes a poor descriptor of the film surface and is dominated by the deep troughs between islands rather than their large, flat tops. The 3-dimensional morphology at this stage of growth would affect in-plane thermal and electronic transport, were this configuration to be employed in a thermoelectric device, because the film is only just becoming continuous. However, our previous work indicates the islands to coalesce and the roughness to improve as more material is deposited to yield a thicker film [11].

To assess epitaxial strain, nanoprobe convergent beam diffraction (CBED) patterns were recorded from each layer in TEM, using a cross-sectional sample of a capped film. CBED patterns from the MgO, V and TiNiSn layers are presented in Fig. 2(d-f) respectively, alongside their RHEED counterparts. Lattice parameters are calculated by measuring the disc separations in each pattern, using a Hough transform algorithm to locate the discs, as implemented in the CrysTBox software [33,34], and calibrated against *200* reciprocal lattice vector for MgO at room temperature (0.4751 Å^{-1}). From this comparison, we find that the corresponding reciprocal lattice vectors in vanadium and TiNiSn have values of 0.4747 Å^{-1} and 0.4756 Å^{-1} respectively, translating to real-space lattice parameters of 2.979 Å and 5.947 Å. This indicates only slight relaxation of the epitaxial relationship, of 0.05% between vanadium and MgO, and 0.18% between TiNiSn and vanadium, implying a compressive strain for vanadium and a small tensile strain for TiNiSn. (By comparison, bulk materials would have lattice mismatches of 1.5% and −1.9% respectively.)

Turning to STEM characterisation, Fig. 3 presents an analysis of a cross-section through a MgO/V/TiNiSn sample with a protective Pt capping layer and where ~ 5 nm of V was deposited at 623 K and ~ 25 nm of TiNiSn was deposited at 723 K, as described above. Fig. 3(a) presents a low-magnification STEM bright field (BF) image which clearly shows the trapezoidal, island-like features of the TiNiSn layer atop a uniform and continuous vanadium layer. The faceted surface structure of the TiNiSn layer is similar to that described previously [11] for films without a buffer layer and is consistent with a 3-dimensional island growth mechanism that explains the high value of AFM-measured RMS roughness, which was dominated by the gaps between islands rather than the flat tops of islands themselves. A higher magnification bright field image at the V nanolayer in Fig. 3(b) shows the interfaces with atomic resolution, providing direct confirmation of the epitaxial relationship. The crystal is aligned along a (1 0 0) direction so that columns of atoms, appearing as bright spots, are arranged in square symmetry that continues uninterrupted from the MgO substrate through the V layer, both of which have generally uniform contrast across Fig. 3(a). Similar trends are evident in the relationship between the V and TiNiSn layers, although the structure and orientation of the TiNiSn unit cell produces a more complex pattern of atomic columns in Fig. 3b. There are more noticeable contrast variations running throughout the TiNiSn, which, as before, we attribute to minor thickness variations in the cross section and slight misalignment of crystalline regions that nucleated separately on the V and may be separated by dislocation defects: these contrast variations are minor and cannot be accounted for by a loss of epitaxy. Elemental quantification of STEM-EELS data recorded across the nanolayer is presented in Fig. 3(c), presented as line profiles of the elemental concentrations running across the STEM-BF image in Fig. 3(b). Starting at the bottom of the data set, only the oxygen signal was recorded from the MgO and this has been normalised to 50% concentration to account for the Mg content. There is then a clear transition to a region of 100% V and the interface between the MgO and V is approximately 2 nm wide, which is also observed in the sharpness of the contrast variation in Fig. 3(b). This interface width is believed to reflect the roughened nature of the MgO surface while held at high temperature [20]. The interface between the V and the TiNiSn layer is a little wider, which may be accounted for by a combination of V surface roughness, a small degree of implantation during deposition and perhaps a minimal amount of interfacial alloying. Finally, at the top of the dataset, the stoichiometry of the hH is close to the ideal 1:1:1 ratio, with no V detected and negligible O. Critically, the key observations from the STEM-EELS data are the quality of the vanadium nanolayer – which has no discernible oxide content and shows no chemical shift or change in ratio of the V $L_{2,3}$ white lines (not shown), which would indicate a change in oxidation state [35]. In addition, the identical onset of the Ti, Ni and Sn signals and near-ideal stoichiometry indicate that the diffusion of Ti out of the

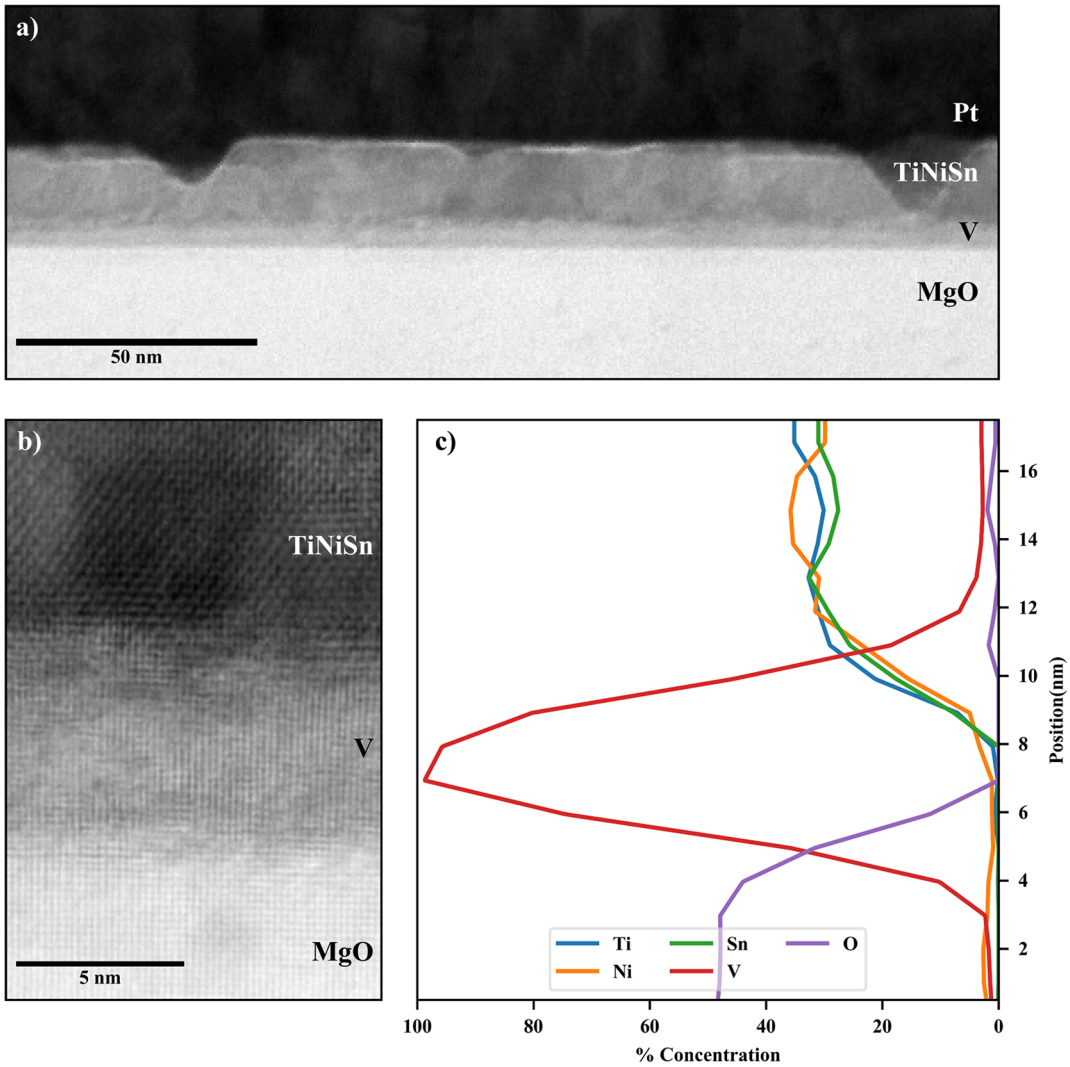

Fig. 3. (a) Low-magnification STEM-BF of a MgO/V/TiNiSn/Pt cross-section. (b) HR-STEM-BF of MgO/V/TiNiSn interface viewed along $[1\,0\,0]_{MgO}$ and (c) composition determined from EELS across that interface. The key result here is the emergence of a clean 1:1:1 TiNiSn Heusler alloy without loss of Ti.

alloy that was observed previously is absent: there is no Ti-rich interface or corresponding Ti-depleted alloy region. The buffer layer has acted as desired.

Finally, Fig. 4 probes in more detail the crystallinity and epitaxy of the thin layer stack. It presents a pair of STEM images which provide high-resolution structural information that can be used to assess defect formation at the interfaces. The high-resolution STEM-BF in Fig. 4(a) shows a small portion of the MgO/V/TiNiSn interfaces, with similar detail to that of Fig. 3(b). It is overlayed, in colour, with the results of a geometric phase analysis of the atomic lattice, which is used to locate strain and dislocations [29]. Regions where the lattice periodicity is disrupted are highlighted in blue. No dislocations are observed in connection to the MgO/V interface in this field of view, while a linear defect density of 0.021 $Å^{-1}$ is found for the V/TiNiSn interface. Fig. 4(b) is a STEM high angle-annular dark field (HAADF) image containing STEM-moiré interference which offers the same information as Fig. 4(a), but on a much larger length-scale [30]. Again, no dislocations are associated with the MgO/V interface across the field of view, which is five times greater than in Fig. 4(a). The lack of evidence for dislocations on such a length-scale is in agreement with the diffraction data and indicates excellent quality epitaxial, largely unrelaxed growth of vanadium on MgO. A small number of defects are again observed to originate at the V/TiNiSn interface in the larger field of view of Fig. 4(b), this time with a calculated linear defect density of $4.2\text{x}10^{-3}$ $Å^{-1}$. The significant difference in the dislocation densities found between the high and low-resolution images suggests the dislocations are not uniformly distributed and that the 0.18% epitaxial mismatch between vanadium and TiNiSn seen in RHEED is compensated through sparse, small clusters of dislocations relieving the tensile epitaxial strain and resulting in a hH thin film that is only slightly relaxed.

As discussed earlier, the vanadium buffer layer is deposited at a temperature 100 K lower than the TiNiSn thin film and there were concerns about the integrity of the buffer layer upon annealing, notably through oxidation, amorphisation or alloying, particularly given the propensity of Heusler alloys to incorporate a large range of elements into their structures [18,36]. The evidence we have presented shows no cause for concern on any of these matters: the film remains metallic, crystalline and immobile. The latter may simply be a consequence of the rather low temperature range studied here, which is substantially below the melting point of metallic V and so will restrict V mobility. This is pertinent when considering the application of the vanadium layer as an adhesion layer or passivating coating, as mobility of the vanadium would have a deleterious effect on the hH stoichiometry and could unintentionally lead to some form of phase segregation, which is known to have an impact on the thermoelectric efficiency of these materials [2].

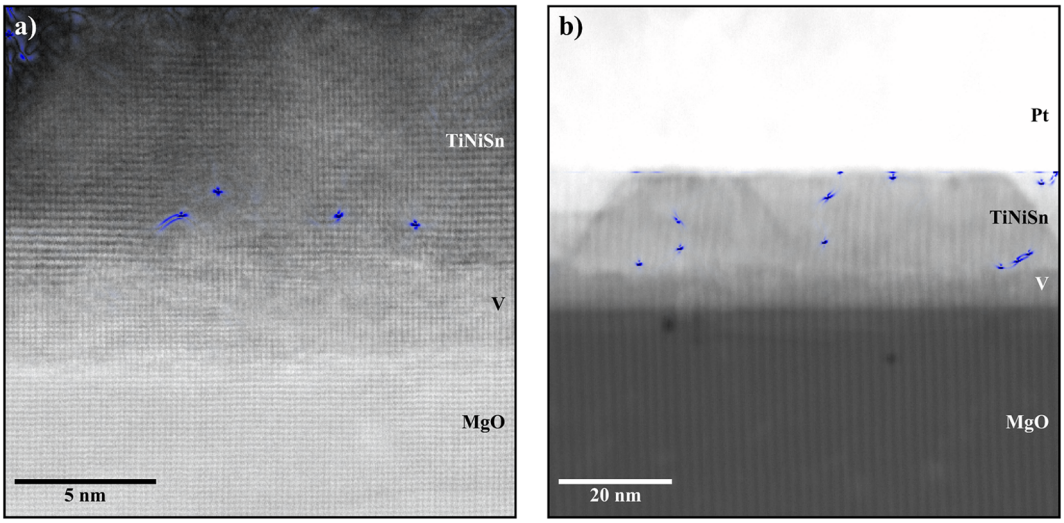

Fig. 4. (a) HR-STEM-BF showing close-up of vanadium interfaces with atomic resolution viewed along $[1\,0\,0]_{MgO}$ and (b) lower magnification STEM-HAADF image containing STEM-moiré fringes. Colour contrast overlaid on images derives from differential phase maps from geometric phase analysis (GPA), where the singular points of blue denote a phase inversion indicative of dislocation sites.

4. Conclusions

We have demonstrated the epitaxial growth of nanoscale layers of vanadium on single-crystal MgO, and its application as a buffer layer for the growth of epitaxial TiNiSn. The minimal lattice mismatch between MgO and vanadium allows growth of vanadium films which are epitaxially strained and there is no evidence of structural compensation by defect formation in the vanadium nanolayer. The 5 nm vanadium layer acts successfully as a barrier to titanium diffusion, resulting in a more uniform composition during the initial growth of TiNiSn. The half-Heusler layer is shown to still grow epitaxially atop the vanadium layer and supports the 0.18% mismatch by forming a low density of dislocations. Critically, there is no discernible oxidation, amorphisation or alloying of the V below 720 K at least and the nature of the half-Heusler layer is uncompromised. We envisage these results will be of relevance to other Heusler alloys which contain a gettering element whose presence is problematic. The results also suggest that vanadium may be an appropriate passivating coating for TiNiSn thermoelectric elements, as an external protection against oxidation and as an insertion layer to prevent deleterious alloying with electrode contacts under typical working conditions.

CRediT authorship contribution statement

R.W.H. Webster: Conceptualization, Methodology, Formal analysis, Investigation, Data curation, Writing - original draft, Writing - review & editing, Visualization. **M.T. Scott:** Methodology, Validation, Formal analysis, Investigation, Writing - review & editing. **S.R. Popuri:** Resources. **J.W.G. Bos:** Resources, Writing - review & editing. **D.A. MacLaren:** Conceptualization, Methodology, Writing - review & editing, Supervision, Project administration.

Declaration of Competing Interest

The authors declare that they have no known competing financial interests or personal relationships that could have appeared to influence the work reported in this paper.

Acknowledgements

This work was funded by the Engineering and Physical Sciences Research Council of the UK through Grant Nos. EP/N017218/1, EP/N509668/1 and EP/N01717X/1.

Appendix A. Supplementary material

Supplementary data to this article can be found online at https://doi.org/10.1016/j.apsusc.2020.145649. The raw data for this article can be found online at https://doi.org/10.5525/gla.researchdata.958.

References

[1] J.E. Douglas, C.S. Birkel, M.-S. Miao, C.J. Torbet, G.D. Stucky, T.M. Pollock, R. Seshadri, Enhanced thermoelectric properties of bulk TiNiSn via formation of a $TiNi_2Sn$ second phase, Appl. Phys. Lett. 101 (2012) 183902, , https://doi.org/10.1063/1.4765358.
[2] J.E. Douglas, C.S. Birkel, N. Verma, V.M. Miller, M.-S. Miao, G.D. Stucky, T.M. Pollock, R. Seshadri, Phase stability and property evolution of biphasic Ti-Ni-Sn alloys for use in thermoelectric applications, J. Appl. Phys. 115 (2014) 43720, https://doi.org/10.1063/1.4862955.
[3] K. Kirievsky, Y. Gelbstein, D. Fuks, Phase separation and antisite defects in the thermoelectric TiNiSn half-Heusler alloys, J. Solid State Chem. 203 (2013) 247–254, https://doi.org/10.1016/j.jssc.2013.04.032.
[4] S.A. Barczak, J.E. Halpin, J. Buckman, R. Decourt, M. Pollet, R.I. Smith, D.A. MacLaren, J.-W.G. Bos, Grain-by-grain compositional variations and interstitial metals—a new route toward achieving high performance in half-heusler thermoelectrics, ACS Appl. Mater. Interfaces 10 (2018) 4786–4793, https://doi.org/10.1021/acsami.7b14525.
[5] S. Barczak, J. Buckman, R. Smith, A. Baker, E. Don, I. Forbes, J.-W. Bos, Impact of interstitial Ni on the thermoelectric properties of the half-heusler TiNiSn, Materials (Basel) 11 (2018) 536, https://doi.org/10.3390/ma11040536.
[6] Yinglu Tang, Xiaoshuang Li, Lukas H.J. Martin, Eduardo Cuervo Reyes, Toni Ivas, Christian Leinenbach, Shashwat Anand, Matthew Peters, G. Jeffrey Snyder, Corsin Battaglia, Impact of Ni content on the thermoelectric properties of half-Heusler TiNiSn, Energy Environ. Sci. 11 (2) (2018) 311–320, https://doi.org/10.1039/C7EE03062B.
[7] W. Ren, H. Zhu, J. Mao, L. You, S. Song, T. Tong, J. Bao, J. Luo, Z. Wang, Z. Ren, Manipulation of Ni Interstitials for Realizing Large Power Factor in TiNiSn-Based Materials, Adv. Electron. Mater. 5 (2019) 1900166, https://doi.org/10.1002/aelm.201900166.
[8] R.A. Downie, D.A. MacLaren, J.-W.G. Bos, Thermoelectric performance of multi-phase XNiSn (X = Ti, Zr, Hf) half-Heusler alloys, J. Mater. Chem. A 2 (2014) 6107–6114, https://doi.org/10.1039/C3TA13955G.
[9] A. Berche, P. Jund, Oxidation of half-Heusler NiTiSn materials: Implications for thermoelectric applications, Intermetallics. 92 (2018) 62–71, https://doi.org/10.1016/J.INTERMET.2017.09.014.
[10] W.G. Zeier, J. Schmitt, G. Hautier, U. Aydemir, Z.M. Gibbs, C. Felser, G.J. Snyder, Engineering half-Heusler thermoelectric materials using Zintl chemistry, Nat. Rev. Mater. 1 (2016) 16032, https://doi.org/10.1038/natrevmats.2016.32.
[11] R.W.H. Webster, J.E. Halpin, S.R. Popuri, J.-W.G. Bos, D.A. MacLaren, Spontaneous formation of nanostructures during pulsed laser deposition of epitaxial half-Heusler TiNiSn on MgO(001), APL Mater. 7 (2019) 013206, , https://doi.org/10.1063/1.5052361.
[12] T. Suzuki, R. Souda, Interfacial reaction during thin film growth of Ti on the MgO

(001) surface, J. Phys. Chem. B 103 (1999) 5747–5749, https://doi.org/10.1021/JP983984B.
[13] Y. Huttel, E. Navarro, A. Cebollada, Epitaxy and lattice distortion of V in MgO/V/MgO(0 0 1) heterostructures, J. Cryst. Growth. 273 (2005) 474–480, https://doi.org/10.1016/J.JCRYSGRO.2004.09.051.
[14] A. Rajanikanth, T. Hauet, F. Montaigne, S. Mangin, S. Andrieu, Magnetic anisotropy modified by electric field in V/Fe/MgO(001)/Fe epitaxial magnetic tunnel junction, Appl. Phys. Lett. 103 (2013) 062402, , https://doi.org/10.1063/1.4817268.
[15] T. Jaeger, Thermoelectric properties of TiNiSn and Zr 0.5 Hf 0.5 NiSn thin films and superlattices with reduced thermal conductivities, Johann. Gutenberg Univ. Mainz (2013).
[16] J.K. Kawasaki, T. Neulinger, R. Timm, M. Hjort, A. a. Zakharov, A. Mikkelsen, B.D. Schultz, C.J. Palmstrøm, C.J. Palmstrøm, Epitaxial growth and surface studies of the Half Heusler compound NiTiSn (001), J. Vac. Sci. Technol. B Microelectron. Nanom. Struct. 31 (2013) 04D106. doi:10.1116/1.4807715.
[17] R.A. Downie, D.A. MacLaren, R.I. Smith, J.W.G. Bos, Enhanced thermoelectric performance in TiNiSn-based half-Heuslers, Chem. Commun. 49 (2013) 4184, https://doi.org/10.1039/c2cc37121a.
[18] C. Felser, A. Hirohata, eds., Heusler Alloys, Springer International Publishing, Cham, Switzerland, 2016. doi:10.1007/978-3-319-21449-8.
[19] C. Duriez, C. Chapon, C.R.R. Henry, J.M.M. Rickard, Structural characterization of MgO(100) surfaces, Surf. Sci. 230 (1990) 123–136, https://doi.org/10.1016/0039-6028(90)90021-Y.
[20] T. Gotoh, S. Murakami, K. Kinosita, Y. Murata, Surface Rumpling of MgO(001) Deduced from Changes in RHEED Kikuchi Pattern. I. Experimental, J. Phys. Soc. Japan. 50 (1981) 2063–2068, https://doi.org/10.1143/JPSJ.50.2063.
[21] M. Schaffer, B. Schaffer, Q. Ramasse, Sample preparation for atomic-resolution STEM at low voltages by FIB, Ultramicroscopy. 114 (2012) 62–71, https://doi.org/10.1016/J.ULTRAMIC.2012.01.005.
[22] J. Scott, P.J. Thomas, M. MacKenzie, S. McFadzean, J. Wilbrink, A.J. Craven, W.A.P. Nicholson, Near-simultaneous dual energy range EELS spectrum imaging, Ultramicroscopy. 108 (2008) 1586–1594, https://doi.org/10.1016/j.ultramic.2008.05.006.
[23] C. Jeanguillaume, C. Colliex, Spectrum-image: The next step in EELS digital acquisition and processing, Ultramicroscopy. 28 (1989) 252–257, https://doi.org/10.1016/0304-3991(89)90304-5.
[24] J. Bobynko, I. MacLaren, A.J. Craven, Spectrum imaging of complex nanostructures using DualEELS: I. digital extraction replicas, Ultramicroscopy. 149 (2015) 9–20, https://doi.org/10.1016/j.ultramic.2014.10.014.
[25] A.J. Craven, J. Bobynko, B. Sala, I. MacLaren, Accurate measurement of absolute experimental inelastic mean free paths and EELS differential cross-sections, Ultramicroscopy. 170 (2016) 113–127, https://doi.org/10.1016/j.ultramic.2016.08.012.
[26] A.J. Craven, B. Sala, J. Bobynko, I. MacLaren, Spectrum imaging of complex nanostructures using DualEELS: II Absolute quantification using standards, Ultramicroscopy 186 (2018) 66–81, https://doi.org/10.1016/J.ULTRAMIC.2017.12.011.
[27] R.F.F. Egerton, Electron energy-loss spectroscopy in the electron microscope, Springer, US, Boston MA (2011), https://doi.org/10.1007/978-1-4419-9583-4.
[28] J. Peters, Strain+ +, (2017). https://jjppeters.github.io/Strainpp/.
[29] M.J. Hÿtch, E. Snoeck, R. Kilaas, Quantitative measurement of displacement and strain fields from HREM micrographs, Ultramicroscopy. 74 (1998) 131–146, https://doi.org/10.1016/S0304-3991(98)00035-7.
[30] A.B. Naden, K.J. O'Shea, D.A. MacLaren, Evaluation of crystallographic strain, rotation and defects in functional oxides by the moiré effect in scanning transmission electron microscopy, Nanotechnology. 29 (2018) 165704, , https://doi.org/10.1088/1361-6528/aaae50.
[31] P. Bencok, S. Andrieu, P. Arcade, C. Richter, V. Ilakovac, O. Heckmann, M. Vesely, K. Hricovini, Growth of vanadium ultrathin films on Fe(100) studied by RHEED, Surf. Sci. 402 (1998) 327–331, https://doi.org/10.1016/S0039-6028(98)00009-0.
[32] M. Gutsche, H. Kraus, J. Jochum, B. Kemmather, G. Gutekunst, Growth and characterization of epitaxial vanadium films, Thin Solid Films 248 (1994) 18–27, https://doi.org/10.1016/0040-6090(94)90204-6.
[33] M. Klinger, M. Němec, L. Polívka, V. Gärtnerová, A. Jäger, Automated CBED processing: Sample thickness estimation based on analysis of zone-axis CBED pattern, Ultramicroscopy. 150 (2015) 88–95, https://doi.org/10.1016/j.ultramic.2014.12.006.
[34] M. Klinger, More features, more tools, more CrysTBox, J. Appl. Crystallogr. 50 (2017) 1226–1234, https://doi.org/10.1107/S1600576717006793.
[35] O.L. Krivanek, J.H. Paterson, ELNES of 3d transition-metal oxides: I Variations across the periodic table, Ultramicroscopy. 32 (1990) 313–318, https://doi.org/10.1016/0304-3991(90)90077-Y.
[36] T. Graf, C. Felser, S.S.P. Parkin, Simple rules for the understanding of Heusler compounds, Prog. Solid State Chem. 39 (2011) 1–50, https://doi.org/10.1016/j.progsolidstchem.2011.02.001.